REGULAR PAPER

Prediction Model for Edge Effects in Magnetorheological Finishing Based on Edge Tool Influence Function

Minwoo Jeon[1,2] · Seok-Kyeong Jeong[1,2] · Jong-Gyun Kang[2] · Woo-Jong Yeo[1,2] · Young-Jae Kim[1] · Hwan-Jin Choi[1,2] · Wonkyun Lee[2]

Abstract

In the optical manufacturing industry, magnetorheological finishing (MRF) is widely known as a deterministic process because of its subsurface damage removal performance and high-level performance of figure correction. However, similar to other optical manufacturing methods that belong to computer-controlled polishing, MRF faces the edge effect, in which the workpiece edge is rolled up or down. As the edge effect lowers the performance of optical components, it should be improved to ensure the final performance of the optical system. In this study, the edge tool influence function (TIF) obtained when the normal TIF was suspended from the workpiece edge was analyzed, and the distortion of the TIF occurring at the edge was explained. The edge TIFs with different overhang distances and polishing parameters, such as step height of raster scan path and swipe speed of TIF, were combined to present a new mathematical model for predicting the edge effect occurring after MRF. To verify the feasibility of the proposed prediction model, the edge effect generated by the uniform polishing of the entire surface of the electroless nickel was compared and analyzed with the edge effect predicted by the proposed model. The relative error of the edge effect generated according to the polishing conditions and the edge effect predicted using the proposed model was calculated to be 4–7%, and the validity of the proposed model was experimentally verified.

Keywords Optical manufacturing · Magnetorheological finishing · Tool influence function · Precision machining · Machining process simulation

List of symbols

C_p'	Modified Preston constant
D_s	Step height
Δ	Relative error
Δd	Overhang interval
E_m	Edge effect measured
E_p	Edge effect predicted
H_d	Deepest height of tool influence function
L_i	Length created by the inlet area of MR fluid
L_o	Length created by the outlet area of MR fluid
L_t	Total length of tool influence function
m	Lateral position from the edge to the center on the workpiece
n	Overhang distance
s	Relative speed of the wheel and the workpiece
t	Time
T_d	Dwell time
τ	Local shear stress
V_s	Swipe speed
W_t	Total width of tool influence function
z	Surface height

✉ Wonkyun Lee
   wklee@cnu.ac.kr

[1] Division of Scientific Instrumentation and Management, Korea Basic Science Institute, Daejeon 34133, Republic of Korea

[2] School of Mechanical Engineering, Chungnam National University, Daejeon 34134, Republic of Korea

1 Introduction

Recently, the demand for high-quality optical surfaces in ultraprecision optical systems has been increasing. Therefore, ultraprecision technologies for figuring and finishing optical surfaces with high efficiency are being developed rapidly [1]. Many finishing techniques, such as chemical–mechanical polishing (CMP) [2], precision grinding [3], and abrasive belts [4], have been studied. However, these techniques have a limited ability to produce rotationally asymmetrical surfaces. Further, subsurface damage

can occur owing to the high vertical loads and the high temperature of the workpiece. Moreover, there is a need for a dedicated polishing tool with a shape suitable for the required optical surface. Because the shape of polishing tools changes over time, periodic readjustment is essential to achieve consistent efficiency for material removal. Therefore, these production technologies do not provide a flexible, cost-effective process for complex and high-performance targets. Computer-controlled polishing (CCP) is one of the latest technologies developed to overcome the drawbacks of conventional fabrication processes, thereby enabling the fabrication of complex surfaces [5]. In addition, the small contact area between the polishing tool and the workpiece surface has the advantage of localized material removal, which can achieve high-quality results and increase production economy. One of the typical CCP techniques is magnetorheological finishing (MRF) [6]. MRF is a promising technique for figuring and finishing the target surface based on the interaction with the workpiece. A magnetorheological (MR) fluid affected by a magnetic field works as a polishing tool. MRF is a deterministic material removal method that prevents subsurface damage and facilitates the uniform convergence of surface errors because the vertical load applied to the workpiece by a single abrasive particle is only about 10^{-7} N [7]. Therefore, MRF shows great potential for ultraprecision production processes. However, similar to other optical manufacturing methods belonging to CCP, MRF faces the edge effect, in which the workpiece edge is rolled up or down. The edge effect generally occurs when a polishing tool overhangs the outer area of the workpiece, resulting in a reduced contact area and excessive pressure on the workpiece [8]. The result is an unpredictable nonlinear pressure distribution and a time-varying tool influence function (TIF). Since the edge effect adversely affects the performance of optical components, it should be improved to ensure the final performance of the optical system.

Over the past few decades, the modeling of material removal properties generated by the interaction between machining tools and workpieces has played an important role in predicting TIF and edge effects. According to the Preston equation [9], which is a classic model for predicting the material removal rate (MRR) of TIF in CMP, the amount of polishing is proportional to the pressure applied by the polishing tools. Based on this theory, studies on the material removal characteristics of various processes have been reported. Wagner and Shannon [10] proposed a theoretical pressure distribution model based on the force and momentum equation, in which negative pressure distribution existed. To improve this negative pressure distribution, Luna-Aguilar et al. [11] proposed a skin model with a nonlinear pressure distribution by subdividing the contact area into two areas: a continuously increasing pressure area and a constant pressure area. However, this model required

that workpieces and polishing tools be square. Cordero-Davila et al. [12] modified the model so that workpieces and polishing tools were circular. However, their study lacked experimental evidence. Subsequently, the parametric model presented by Kim et al. [13] applied five predictive parameters and accurately predicted the rolled-off edge based on empirical data. Liu et al. [14] developed variable optimization methods and pressure distribution models to verify the consistency of edge TIFs in computer-controlled active labs based on finite element analysis. However, these two studies are difficult to apply to high-level manufacturing processes for a complex target, such as rotationally asymmetrical figure error. Since figure correction process for rotationally asymmetrical figure error in a local area is essential to reach high optical precision, large-sized tools are difficult to correct the figure error in a small area. The above studies have been proved effective in predicting TIF and edge effects in the fabrication process of optical components. However, they do not provide solutions for targets with complex figures and shapes. The material removal function in MRF is rotationally asymmetrical because the rotating direction of the magnetorheological (MR) wheel and the surface of the workpiece are perpendicular to each other. This relationship provides the basis for the effective fabrication of rotationally asymmetrical figures. Shorey [15] measured the force in the MRF and reported that the MRR of the TIF was more controlled by the drag force than by the normal force. Based on Shorey's work, Degroote et al. [16] introduced a comprehensive model for predicting the MRR of TIF, including terms for the mechanical properties of glass and abrasives. In their study, MRR was defined as a function of drag force. Miao et al. [17] showed that the MRR of TIF has a positive dependence on shear force. Kum et al. [18] proposed a model for the MRR of TIF through an experimental approach in which MRR is strongly correlated with tangential force. These studies have proved that the MRR of TIF is dominantly influenced by shear force. However, these studies do not explain how shear force is applied to the edge of the workpiece as the contact area between the TIF and the workpiece changes. Therefore, further experimental verification to explain the distortion of TIF is necessary. Hu et al. [19] studied the edge effect of MRF based on the small TIF and edge TIF compensation methods. Their method is effective in fabricating a mirror with a rotationally asymmetrical shape, such as hexagonal and square. However, small TIFs dramatically increase polishing time. It is difficult to apply when the desired surface is rotationally asymmetrical, such as a de-wedged off-axis mirror and XY-polynomial-based mirror, because it is based on a spiral scan path. Zhong et al. [20] studied the edge TIF stability of MRF and the post-correcting algorithm for the edge. Their method is based on a bidirectional scan path that can effectively polish rotationally asymmetrical

surfaces, and the proposed edge post-correcting algorithm is applied to specific optics to control the surface figure stably. The above studies have shown the feasibility of mitigating the edge effect. However, since the change in the MRR of TIF according to the contact area distortion at the edge is hardly considered, it is difficult to achieve process accuracy for high-quality optical components with complex surfaces. Therefore, research on the correlation between edge TIF and edge effect still needs to be improved.

In this study, in order to elucidate the correlation between edge TIF and edge effect, the volume of the edge TIF generated when the MRF TIF was overhanging the edge of the workpiece was quantitatively compared with the volume of the normal TIF generated when the MRF TIF remained inside the workpiece. It was revealed that the distortion of the contact area between the TIF and the surface induced a change in the shear force participating in material removal and created a rolled-off characteristic at the edge of the workpiece. Based on the edge TIF, we developed a new mathematical model for predicting the edge effect according to polishing parameters, such as step height of the raster scan path and swipe speed of the TIF. Through the uniform removal process, in which the entire workpiece surface was uniformly polished along the raster scan path, the edge effects generated under the given polishing conditions and the edge effects predicted based on the proposed mathematical model were quantitatively compared. As a result, the feasibility of the proposed model was experimentally verified. This study contributes to the literature related to the production technology in the form of research findings that can help improve the precision of the manufacturing process for the optical component. In particular, we experimentally verified the effect of shear force on the edge of the workpiece as the contact area between the TIF and the workpiece is changed during the MRF process. In addition, the correlation between edge TIF and edge effect is explained by presenting the prediction model based on the MRR change of TIF according to the distortion of the contact surface. These results could contribute to the efficient production of large and complex optical components with high quality because the model directly predicts the edge effect that will occur.

2 Parametric Model for Edge Effects

2.1 MRF and Influence Function

CCP is well-known as a state-of-the-art technology, such as MRF, capable of producing complex optical surfaces and satisfying high-quality specifications [21]. Because CCP has a small contact area between the tool and the workpiece, the workpiece error can be controlled locally. While the polishing tool moves along the optical surface, material removal is controlled by changes in the dwell time of the tool [22]. The slower the tool moves, the more material is removed, and the faster the tool moves, the less material is removed. The dwell map of the CCP tool moving along the surface of the workpiece is an important management factor in achieving target removal. Since the optimized dwell map depends on the deconvolution process of target removal using TIF, one of the most important factors for successful CCP is an accurate TIF [23]. MRF, which is one of the CCP techniques, is a process of manufacturing an optical component using a MR fluid as a polishing tool. The MR fluid consists of carbonyl iron (CI), an abrasive, and other stabilizers. The MR fluid normally behaves as a Newtonian fluid but, when affected by an appropriate magnetic field, it rapidly changes to a Bingham fluid state, and the viscosity and yield stress rapidly increase [24]. MR fluid converted to a high-viscosity state can generate enough stress to polish the workpiece, and material is removed by contacting the surface of the workpiece in the flow direction. MRF uses a shear-based material removal mechanism rather than the pressure-based material removal mechanism commonly found in conventional polishing processes. Unlike the general polishing process, since only a very slight force, which is the sum of hydraulic pressure and magnetic buoyancy, acts perpendicular to the target surface, it does not penetrate further into the subsurface damage and improves the surface quality.

The schematic diagram of the MRF equipment used in this study is shown in Fig. 1. The fluid storage is an area that is not affected by a magnetic field, and CI particles and abrasives are randomly distributed. In contrast, the CI particles reaching the wheel within the field of influence of the magnetic field are aligned in a chain structure in the same direction as the magnetic field, and the abrasive floats to the outside of the chain structure by buoyancy. The vertical distance from the wheel surface to the surface of the MR fluid is called the MR ribbon. When the workpiece is plunged to an appropriate depth in the MR ribbon, material is removed. The MR fluid suctioned past the wheel surface returns to the fluid storage and goes through the cycle of the steps described above. Figure 2 shows the influence function created when the MR fluid comes into contact with the workpiece and material is removed. Figures 2a and c present the material removal characteristics in the X-axis direction of the influence function. When the MR fluid comes into contact with the workpiece, the material removal characteristics are symmetrical. Figure 2b and d show the material removal characteristics in the Y-axis direction of the influence function, which are different depending on the inlet and outlet of MR fluid based on the material surface. At the inlet of MR fluid, the material surface is removed with a gentle slope, whereas at the outlet of MR fluid, the material surface is removed with a steep slope. Considering the cross-sectional shape when the

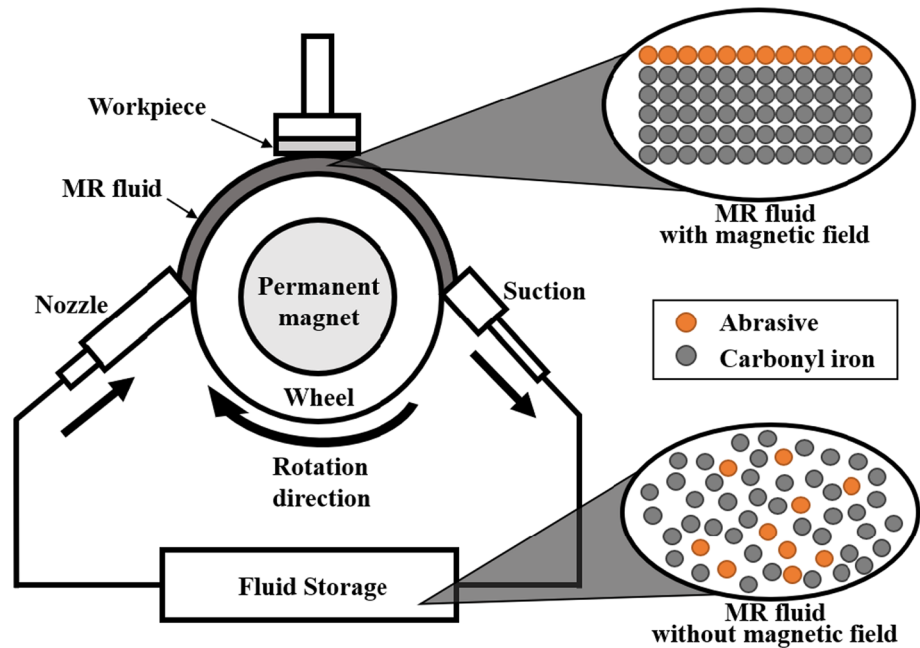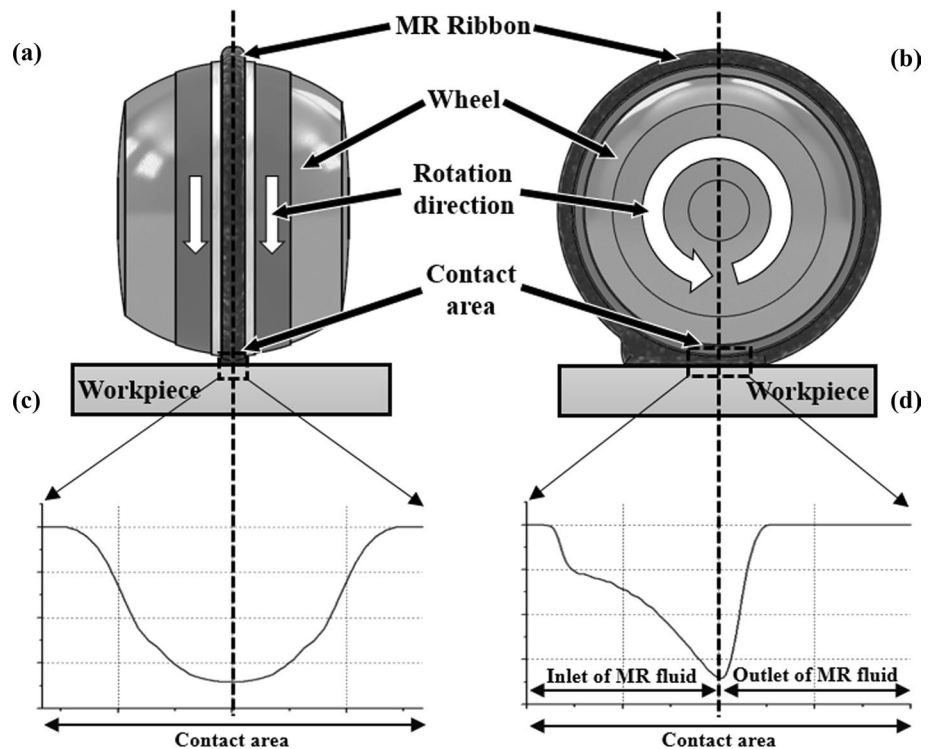**Fig. 1** Schematic diagram of magnetorheological finishing (MRF)

Fig. 2 Schematic diagram of the contact magnetorheological (MR) fluid and workpiece in **a** front view and **b** side view; **c** X-axis line profile and **d** Y-axis line profile of the generated tool influence function (TIF)

MR ribbon is plunged to the surface of the workpiece, the TIF should have an elliptical shape in the XY-direction. However, in the outlet region, the fluid tends to escape the surface, and material is removed with a steep slope in a relatively narrow region compared to the inlet. Therefore, at the inlet of MR fluid, material is removed in the same area as the semimajor axis of the ellipse, whereas at the outlet of MR fluid, material is removed in an area smaller than the semimajor axis of the ellipse. The position where the inlet is switched to the outlet is the highest point of the wheel, where the deepest point of the influence function is formed. As a result, the influence function of MRF is symmetrical on the X-axis and asymmetrical on the Y-axis.

2.2 Cause of Rolled-off Edge and Distortion of TIF

The influence of hydrodynamic shear stress distribution in the MRF process is critical and can be demonstrated by Shorey's material removal theory [25]. The MRR of an MRF process is proportional to the impact coefficient, local shear stress, and relative velocity.

$$\frac{dz}{dt} = C_p' \tau \frac{ds}{dt} \tag{1}$$

where $\frac{dz}{dt}$ represents the removal rate as the workpiece height changes with time, C_p' is the modified Preston constant, τ is the local shear stress, and $\frac{ds}{dt}$ is the relative speed of the wheel and the workpiece. The MRF TIF calculated by Eq. (1) fits well when the TIF remains inside the workpiece [26]. However, when TIF overhangs the edge of the workpiece, it tends to deviate from its nominal behavior because of dramatically varying shear force range, tool distortion, and nonlinear effects [13]. This feature causes the outer surface of the workpiece to be rolled up or down, and a similar phenomenon occurs in many machining processes with a contact material removal mechanism [14]. This phenomenon can be verified experimentally by the quantitative analysis of the amount of TIF distortion at the edge and the effect of the TIF change on the optical surface.

When the workpiece is plunged into the MR ribbon and stays for a certain dwell time, surface material is removed. At this time, the material removal amount (MRA), that is, the amount of removed material, is calculated to define the MRF TIF. The experimental conditions for tracking the shape change of edge TIFs according to the overhang distance are listed in Table 1. The MRF TIF has different material removal characteristics when MR fluid is at the inlet and outlet to the workpiece surface. At the leading edge of the raster path, the outlet area of the MR fluid comes into contact with the workpiece, and the total TIF gradually moves into the workpiece. In contrast, at the trailing edge, the workpiece leaves the outlet area of the MR fluid, and the total TIF gradually moves to the outside of the workpiece. The travel paths of these tools create different TIF distortion characteristics at the leading and trailing edges. When TIF stays inside the workpiece and there is no overhang, the contact area between the MR ribbon and the workpiece is elliptical. At this time, the inlet area of MR fluid removes material of the same size as the semimajor axis of the ellipse, but, in the outlet area of MR fluid, material with size smaller than the semimajor axis is removed, as mentioned in Sect. 2.1. Although the contact area between the MR ribbon and the workpiece is elliptical, the cross-sectional shape of the material actually removed has the candlelight shape. This characteristic appears when the influence function of MRF stays completely on the surface of the workpiece, that is, when there is no overhang. However, in actual raster polishing, the TIF starts and finishes the polishing at the outside of the workpiece for the process stability. This tool movement indicates that the elliptical shape of the plunging area should be considered as the experimental conditions. Therefore, in the leading edge of the raster path, the overhang distance, n, was selected in the range 0 mm ≤ n< 18 mm considering the major axis of the ellipse, which is the cross section of the plunging area. The major axis of the ellipse can be calculated as twice the length created by the inlet of MR fluid in the normal TIF as shown in Table 1. In the trailing edge of the raster path, the outlet area of the MR fluid exits the workpiece surface first, and thus there is no need to consider the semimajor axis plunged by the outlet area of the MR fluid. Since the semimajor axis created by the inlet area of MR fluid is not distorted, the overhang distance, n, at the trailing edge was selected as 0 mm ≤ n< 11.5 mm considering the total length of the TIF.

Table 1 Experimental conditions to verify the distortion of the TIF

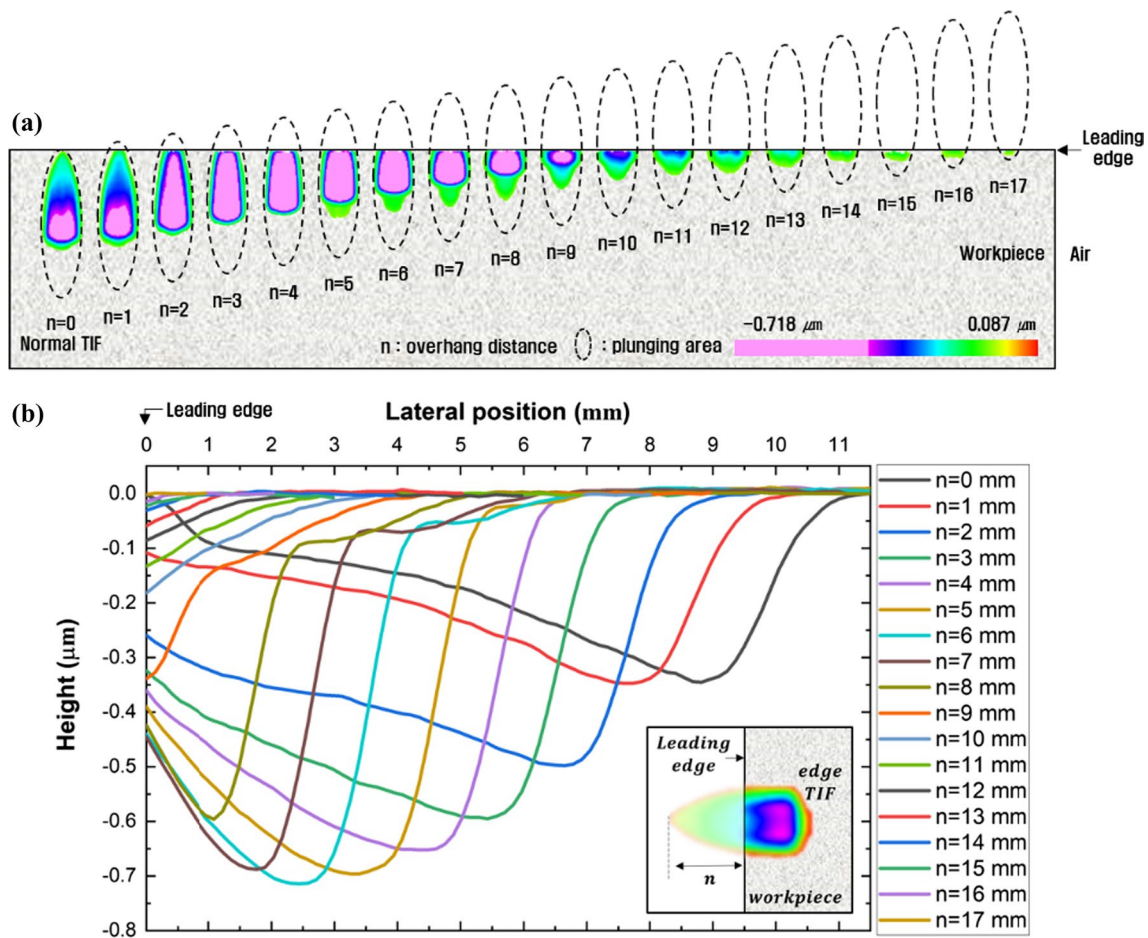|		
Machine parameter	Wheel size	150 mm
	Abrasive	Diamond
	Wheel speed	307 rpm
	Flow rate	0.93 lpm
	Magnetic field	3000 Gs
	Ribbon height	1.58 mm
	Depth of plunge	0.474 mm
	Duration	11 s
TIF	Length generated by the inlet of MR fluid	9.0 mm
	Length generated by the outlet of MR fluid	2.5 mm
	Width of overall TIF	5.0 mm
	Height of the deepest point	308.8 nm
	Volume removal rate	0.0287 mm^3/min

Fig. 3 The change in **a** the shape and **b** the depth of edge TIFs according to the change of the overhang distance at the leading area

Figure 3a shows the experimental results performed to track the area change of the TIFs in the leading area as the overhang distance changes. The candlelight-shaped form with the color map denotes the MRF TIF, and the dotted ellipse denotes the plunging area where the MR ribbon and the workpiece are in contact. Figure 3b presents the overlap of the profiles with respect to the center line of the edge TIFs at the leading edge. The point where the lateral position is 0 mm is the leading edge of the workpiece. The black line with $n = 0$ mm indicates the normal TIF obtained from inside the workpiece without the MRF TIF overhanging the edge. When examining the area formed by the inlet of MR fluid for the TIFs of each edge, the deepest point gradually becomes deeper and the slope tends to become steeper as the overhang distance increases from 0 to 6 mm. The deepest point gradually becomes shallow at $7\ \text{mm} \leq n \leq 9$ mm, and the same depth as that of the deepest point of normal TIF is formed at $n = 9$ mm. In the edge TIFs obtained at $5\ \text{mm} \leq n \leq 9$ mm, additional curvature that did not exist in the normal TIF was observed at the bottom of the edge TIFs. This is caused by distortion

due to the change in the contact area between the MRF TIF and the workpiece surface. It can be defined as a tail effect in consideration of the characteristics occurring in the tail of the TIF. Features such as the deepest point or tail effect did not exist at $10\ \text{mm} \leq n \leq 17$ mm, a relatively small amount of material was removed compared to other edge TIFs, and the depth gradually decreased. The edge TIFs of the leading area obtained experimentally had a distorted shape compared to the normal TIF, and the surface material was excessively polished. Figure 4 shows the volumes of the normal TIF and the edge TIFs according to the change of the overhang distance. The volumes of the calculated normal TIF were calculated based on the area subtracted by the overhang distance from the top of the normal TIF, and the volumes of the experimental edge TIFs were calculated based on the area of the measured edge TIFs. The length of the normal TIF is 11.5 mm, and the calculated normal TIF has no value from the overhang distance of 12 mm. Except for the case where ≤ 1 mm, the experimental edge TIFs removed the material in a volume larger than the calculated normal TIF in all experimental

Fig. 4 Comparison of the removed volumes for the calculated normal TIF and experimental edge TIFs according to the change of the overhang distance at the leading area
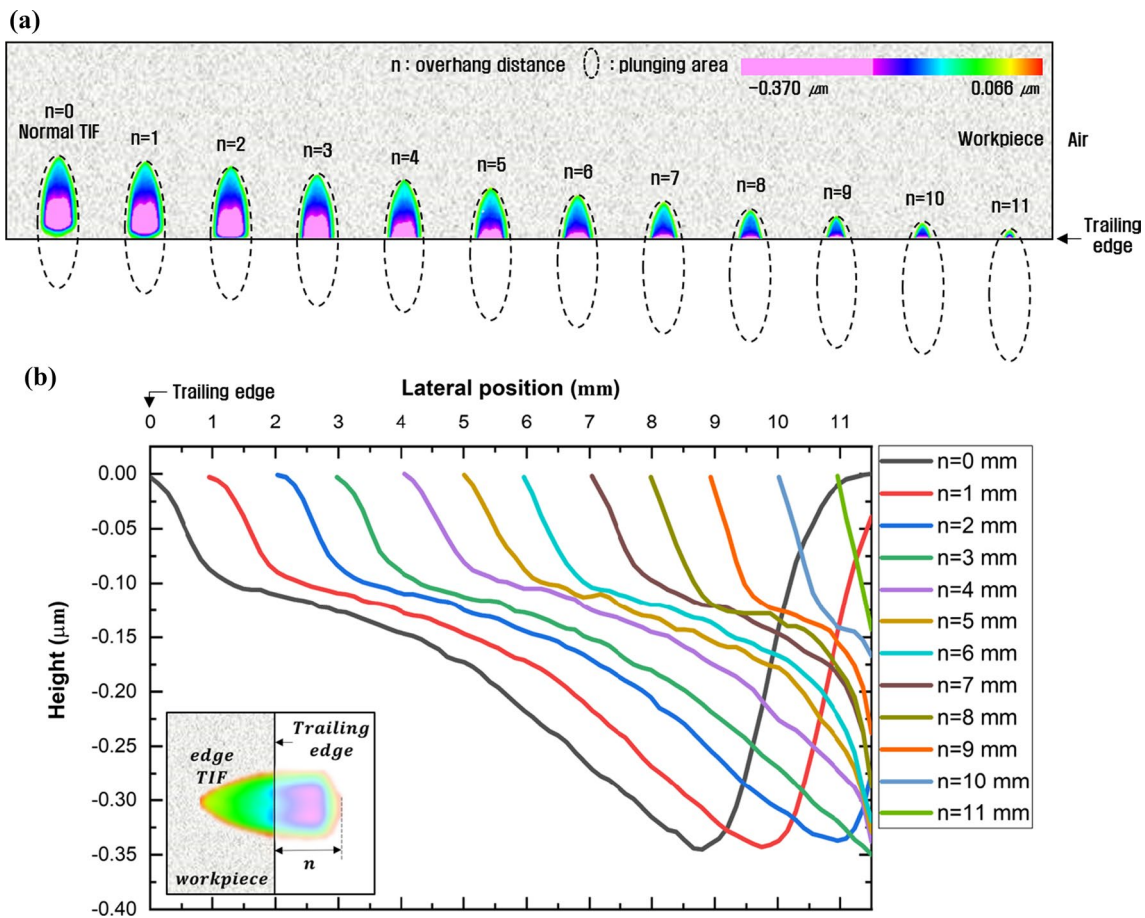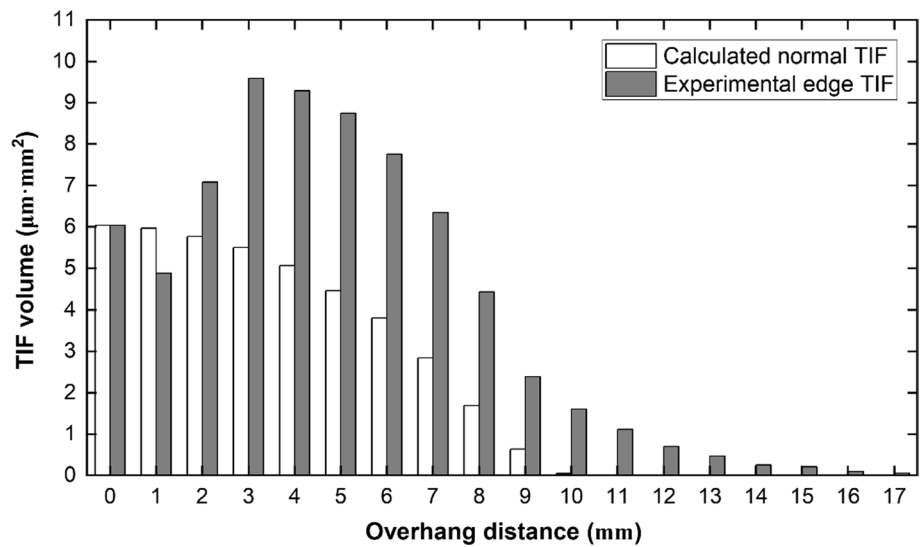

Fig. 5 The change in **a** the shape and **b** the depth of edge TIFs according to the change of the overhang distance at the trailing area

conditions. This result is identified as the cause of generating the overpolished edge when the MRF TIF is overhung at the leading edge.

Figure 5a shows the experimental results performed to track the area change of the TIFs in the trailing area as the overhang distance changes. The candlelight-shaped form

with the color map denotes the edge TIFs at the trailing edge, and the dotted ellipse denotes the plunging area. Figure 5b presents the overlap of the profiles with respect to the center line of the edge TIFs at the trailing edge and the point where the lateral position is 0 mm signifies the trailing edge of the workpiece. Similar to Fig. 3b, the black line with n = 0 mm indicates the normal TIF. As the overhang distance increases, the plunging area gradually moves out of the workpiece. There is no abrupt change of the edge TIFs in the trailing area contrary to the trend observed in the leading area, and the overall shape of the edge TIFs is similar to that of the normal TIFs. And it was observed that as the overhang distance increased, the slope of the cross section of each edge TIF became slightly steeper. Figure 6 shows the volumes of the normal TIF and the edge TIFs according to the change of overhang distance. For each overhang distance, the volume difference between the calculated normal TIF and the experimental edge TIFs was calculated to be about 0.1 $\mu m \cdot mm^2$ on average. In the cases of 0 mm $< n \leq$ 7 mm, the volume difference of 0.1 $\mu m \cdot mm^2$ does not have a significant effect because the volume of edge TIFs is relatively large. But in the cases where 8 mm $\leq n \leq$ 11 mm, the volume of edge TIFs is relatively small, the 0.1 $\mu m \cdot mm^2$ volume difference can generate the excessive overpolished edge.

The change in the contact area between the MR ribbon and the surface implies that the shear force applied to the surface changed, which could be regarded as the cause of the TIF distortion at the edge. Therefore, edge effects occurred only in the edge area of the workpiece, where TIF distortion was present, and not inside the workpiece, where TIF distortion was absent. Because TIF distortion occurred when the TIF overhung the edge of the workpiece, the edge effect depended on the total length of the normal TIF.

2.3 Experimental and Mathematical Simulation

Based on the TIF characteristics of the MRF distorted at the edge, we propose a model for quantitatively predicting the rolled-off edge that occurs during MRF. The edge effect is critically affected by TIF distortion. Under the experimental conditions performed above, all TIFs overhanging the edge of the workpiece were distorted, and edge TIFs had the characteristics of an overpolished surface, in contrast to normal TIFs. In this prediction model, edge TIFs with different overhang distances are divided at a specific interval along the length direction to calculate partial removal volume (PRV), which corresponds to the volume for each divided area. By integrating all PRVs applied to the same lateral position from the edge of the workpiece, the integrated removal volume (IRV), which is the total volume to be removed by the edge TIFs for each lateral position of the workpiece, can be calculated. The calculated IRV is converted to the volume removal rate (VRR), which is the MRR per unit time, because it is more effective to link with the actual polishing process if the time domain is included. The calculated VRR is combined with MRF parameters, such as step height of raster scan and swipe speed of the MR wheel, to calculate the MRA from the workpiece surface after actual MRF polishing. Consequently, the calculated MRA based on the edge TIF can predict the overpolished amount that will occur at the edge. A schematic for the normal TIF of MRF is shown in Fig. 7. The total width of TIF is W_t, the length created by the inlet area of MR fluid is L_i, the length created by the outlet area of MR fluid is L_o, the total length is L_t (i.e., $L_i + L_o$), and the height at the location where most material is removed is H_d.

Edge TIFs obtained according to the overhang distance can be expressed as a function of x, y, and z by Eq. (2). Since the degree of distortion of TIFs is different as the overhang

Fig. 6 Comparison of the removed volumes for the calculated normal TIF and experimental edge TIFs according to the change of the overhang distance at the trailing area
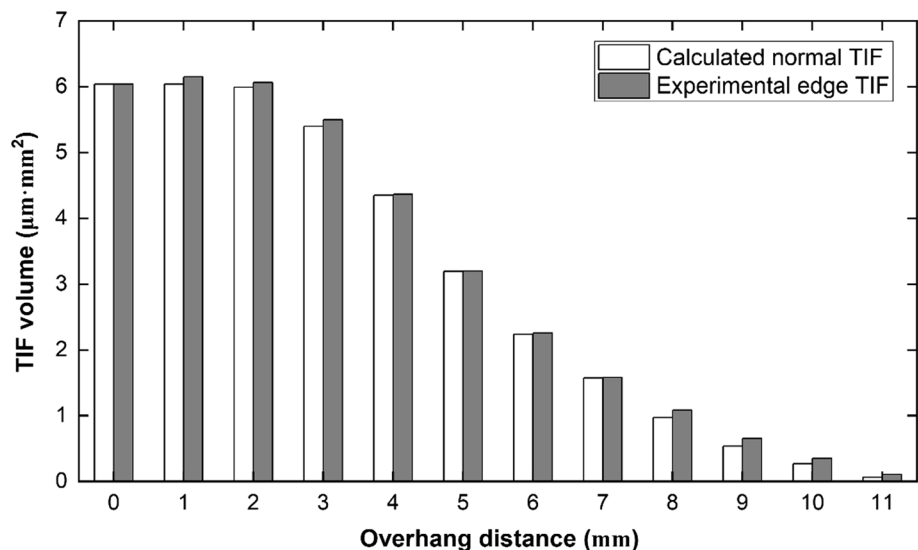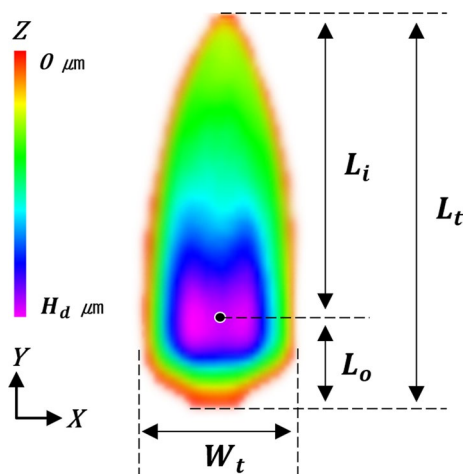
Fig. 7 Schematic illustration of the MRF TIF

Fig. 8 Raster scan path of MRF process

distance changes, edge TIFs are divided into overhang intervals, Δd, along the Y-axis direction to quantitatively express rolled-off edges. PRV (i.e., the volume of material removed in the divided regions) can be expressed by Eq. (3). In this case, α and β define the range of the integral region, and $\alpha = m - \Delta d$ and $\beta = m + \Delta d$, where m denotes the lateral position from the edge of the workpiece to the center; the total length, L_t, of the TIF used in the experiment was decreased by 1 mm. The subscript n of TIF denotes the overhang distance and is defined in the range $-L_t < n < 2L_i$ in the leading area and the range $-L_t < n < L_t$ in the trailing area, both with 1 mm increments. The positive sign in each range indicates the area where TIF is overhung and distorted. The difference between the ranges of the leading and trailing areas is because the material removal characteristics of the inlet and outlet areas of MR fluid are different, as described in Sects. 2.1 and 2.2. The negative sign in each range implies that TIF stays completely inside the workpiece. Thus, the effect of normal TIF is also considered because, even if the TIF is no longer overhung on the edge of the workpiece, the normal TIF on the raster scan path affects the rolled-off edge and passes through it. Therefore, to accurately predict the edge effect, normal TIF should be included in the calculation to a range outside of the edge effect region from edge to L_t. As shown in Eq. (4), the IRV was derived by integrating all the PRVs participating in material removal at the same lateral position, m, among edge TIFs with different overhang distances. The overhang distance, n, increases from $-L_t$ to $2L_i$. This range was selected considering n in the leading area more comprehensive than n in the trailing area. The IRV obtained for each lateral position represents the total volume of overpolished material caused by the distortion of TIF for each position. This volume is the state in which the specific dwell time used in the basic experiment to obtain the edge TIFs is applied. To link it with the actual polishing
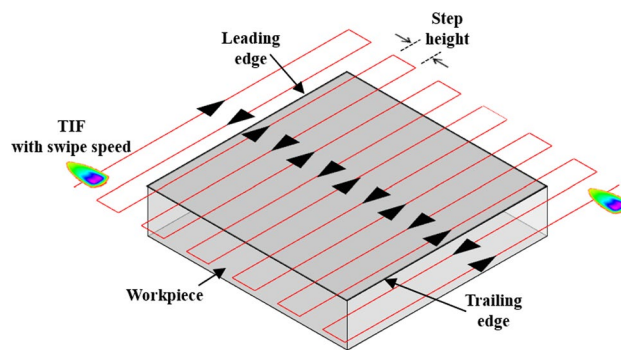
process, it is necessary to convert it into a MRR per unit time. Therefore, VRR is calculated by dividing IRV by the used dwell time, T_d, as shown in Eq. (5).

$$Tool\ Influence\ Function = TIF(x, y, z) \tag{2}$$

$$PRV_n^m = \int_{-W_t/2}^{+W_t/2} \int_{\alpha}^{\beta} \int_{H_d}^{0} TIF_n^m\, dz\, dy\, dx \tag{3}$$

$$IRV^m = \sum_{n=-L_t}^{2L_i} PRV_n^m \tag{4}$$

$$VRR^m = \frac{IRV^m}{T_d} \tag{5}$$

Since TIF is a static element obtained by continuing for a certain period of time at a specific location when the MR fluid and workpiece come into contact, the VRR calculated based on TIF must be divided by the step height of the raster path and the swipe speed of the MR wheel to calculate the precise MRA, including dynamic movement. Finally, to predict the actual edge effect occurring after the MR process, polishing parameters are integrated into VRR to calculate the MRA for each lateral position, as shown in Eq. (6).

$$MRA^m = \frac{VRR^m}{D_s \cdot V_s} \tag{6}$$

where D_s denotes the step height and V_s denotes the swipe speed. During MRF, the step height can be considered as a variable that controls the total amount of polishing by moving the TIF. As shown in Fig. 8, the TIF of MRF passes through the entire surface of the workpiece along the raster scan path with an interval equal to the step height. In general, a total length of several millimeters to several tens of millimeters is used for the TIF of MRF, and a step height of several tens of micrometers to several hundred micrometers is selected. When the step height of the raster path

is determined, it means that the TIF is segmented to the size of the step height. In an arbitrary area of the same size as the step height, the bottom piece of the segmented TIF participates in the polishing first, and the piece just above the bottom piece of the segmented TIF participates in the polishing through the next scan path. All the pieces of the segmented TIF are sequentially applied to the arbitrary area. The material removal process is interpreted as dispersing the total VRR of the TIF in the arbitrary area of the same size as the step height. As a result, as the step height increases, VRR is dispersed over a larger area, and the total amount of polishing decreases accordingly. In contrast, as the step height decreases, VRR is dispersed over a smaller area, and the total amount of polishing increases in an inversely proportional manner. Consequently, the step height may be treated as an important factor in the polishing process. The TIF of the MRF is calculated based on the volume of the material removed while the circulating MR fluid maintains a contact state at a specific location on the surface of the workpiece for a certain period of time. To apply this to the polishing process, the swipe speed (i.e., the speed at which the TIF moves while in contact with the surface of the workpiece) should be considered. VRR is divided by the swipe speed because the total polishing amount and swipe speed are inversely proportional. The total polishing amount decreases if the TIF moves quickly and increases if the TIF moves slowly on the surface of the workpiece. Since Eq. (6) is derived from the TIF volume, it can be used at the edge, where TIF is distorted, and inside, where there is no distortion. Therefore, MRA can be calculated based on the normal TIF in

the inner region, where TIF distortion does not occur, and the edge effect caused by TIF distortion can be calculated based on the edge TIFs obtained from leading and trailing edges. Hence, the entire surface map, including edge effects that occur after polishing, may be directly predicted. Since this mathematical model is a prediction method based on the empirically obtained TIF, it could be applied to various materials without changing the specific coefficient values of the predictive model according to the mechanical properties of the material. In addition, if the environmental conditions inside the laboratory, such as temperature and humidity, are properly maintained, this method could be applied in any laboratory to predict the edge effect of MRF.

2.4 Generation of Edge Effects Based on Predictive Model

The rolled-off width and depth at the edge of the workpiece can be predicted using the edge effect model based on the edge TIFs. The conditions of the normal TIF for simulating the edge effect generated by specific polishing conditions were obtained under the same conditions as those in Table 1 to fit the experimental data of Sect. 2.2. As polishing parameters, four step heights, D_s, were applied—0.160 mm, 0.080 mm, 0.053 mm, and 0.040 mm—and the swipe speed, V_s, was selected to be 30 mm/s in all conditions. The four experimental conditions had MRAs of 100 nm, 200 nm, 300 nm, and 400 nm, respectively, when the TIF remained inside the workpiece, which were calculated by substituting the VRR of the normal TIF into Eq. (6). Figure 9 shows

Fig. 9 Edge effects simulated by the variation in the step height, D_s
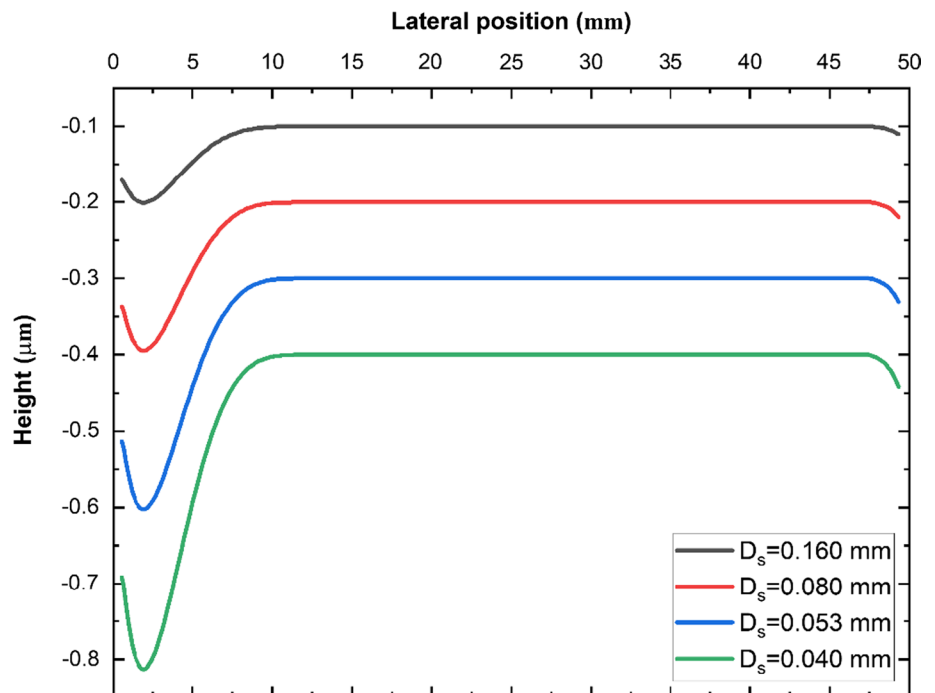
the simulation results for each of the four polishing conditions. The left side of each graph is the leading edge, and the right side is the trailing edge. As D_s increases, the number of times that the TIF is in contact with the workpiece decreases, creating a relatively shallow depth of edge effect. Conversely, when D_s decreases, the number of times that the TIF is in contact with the workpiece increases, creating a relatively deep depth of edge effect. However, even if D_s was changed, no change in the width of the edge effect was observed in both the leading and trailing edges. Considering the distortion degree of the edge TIFs at the leading and trailing edges, the simulation results agreed with the assumption that the edge effect at the leading edge was relatively stronger than that at the trailing edge.

3 Experimental Demonstration for Parametric Model

3.1 Experimental Details

For the experimental verification of the proposed model, MRF equipment (Q-flex 300, QED Technologies, USA) and diamond-based D10 fluid as a commercial product of QED were used. The workpiece was a 7×50-mm electroless nickel plated surface, which composed of high phosphorus deposits (10–13%). As regards the MRF machine parameters and TIF extraction conditions used in the experiment, the values described in Table 1 were applied in the study for continuity. The uniform removal technique was used to uniformly remove the material on the surface. In uniform removal, the TIF moves the entire surface of the workpiece along the raster path with a constant step height and swipe speed, as shown in Fig. 8. As for the polishing parameters used, the swipe speed, V_s, was 30 mm/s, and the step height, D_s, was 0.160 mm, 0.080 mm, 0.053 mm, and 0.040 mm. The edge effect generated on the workpiece surface after MRF was inspected using a Fizeau interferometer (S150, APRE, USA).

3.2 Comparison of Experiment and Simulation

The edge effect characteristics in the leading area and trailing area are different from each other since the TIF of MRF is asymmetrical along the Y-axis. Figures 10 and 11 show the edge effect generated in the leading area and trailing area, respectively. The solid line represents the experimentally measured profiles, and the dotted line depicts the predicted profiles based on the proposed model. Each profile was expressed from 0 (i.e., the edge of the workpiece) to 11.5 mm (i.e., the total length of the normal TIF). The TIF moving from outside to inside the workpiece is not distorted at the specific position where the TIF stays completely inside the workpiece, and the specific position depends on the total length of the TIF. As shown in Fig. 10, the edge effect in the leading area shows a relatively weak rolling down trend from 11.5 mm to about 8.5 mm but a gradually steeper rolling down trend from 8.5 to 1.7 mm. Furthermore, it shows a rolling up trend from 1.7 to 0 mm. As the step height used in the experiment gradually decreases, a strong edge effect is

Fig. 10 Comparison between the predicted edge and the measured edge in leading region
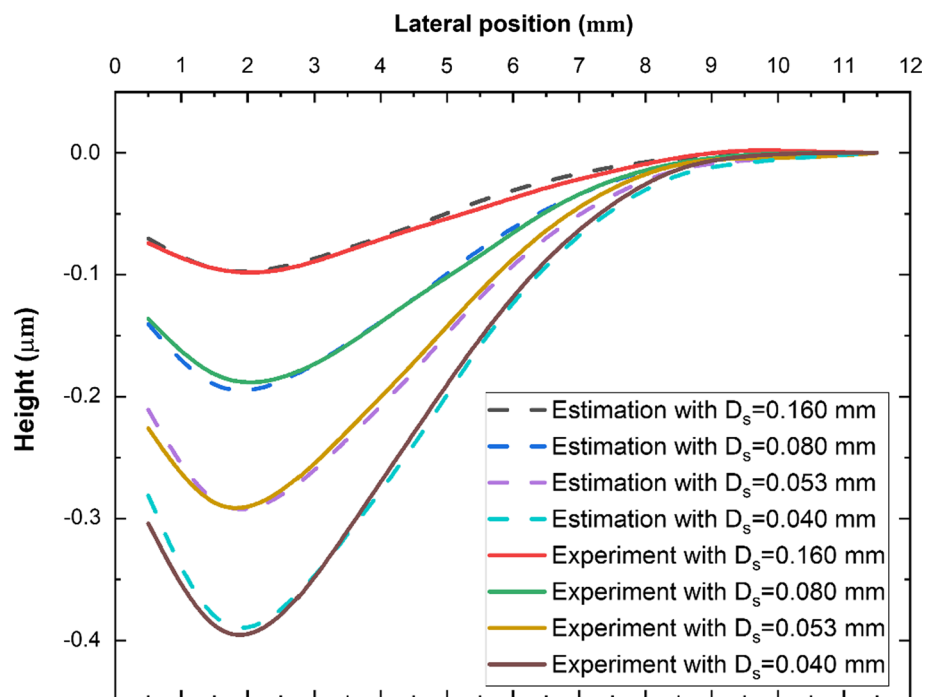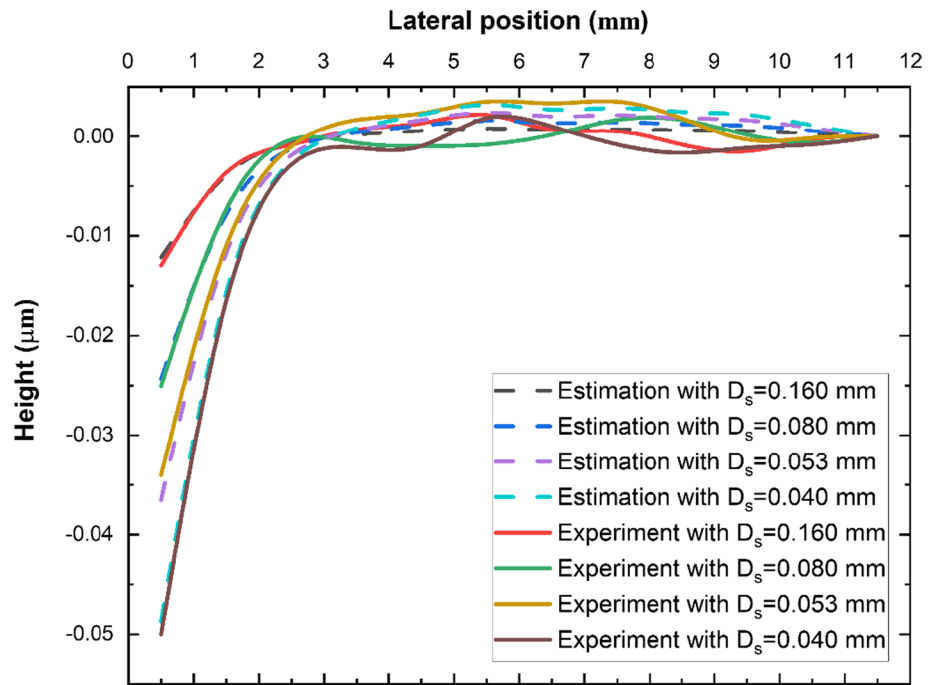
Fig. 11 Comparison between the predicted edge and the measured edge in trailing region

generated in the depth direction. Conversely, the edge effect in the width direction does not change even when the step height is changed. The characteristic that the positive slope and the negative slope coexisted was observed in the leading area. The four dotted lines representing the predicted edge effect fitted well with the rolling down and up tendencies shown by the four polishing results.

Figure 11 shows the edge effects in the trailing area. A steep rolled-down edge effect was found in the region from 0 to 2.5 mm in the lateral position. However, the edge effect hardly occurred in the region from 2.5 to 11.5 mm, and the difference in height between the estimated and measured edge effects tended to be as large as several nanometers compared to the rolled-down area. The prediction of the edge effect using the proposed model was calculated at an interval of 1 mm in the lateral position, and data fitting was performed based on the rolled-down region (0–2.5 mm). This analysis implies that the mismatch may occur in the region (2.5–11.5 mm) excluding the rolled-down feature. In addition, considering that the mismatch is less than 5 nm, it can be expected that the error generated during the measurement process was also included. If the volume extraction interval of edge TIFs is smaller than 1 mm for edge effect prediction, this error characteristic can be improved. As the step height decreased, a strong edge effect was generated in the depth direction, similar to the characteristic in the leading area. Although the tendency is similar, the depth of the edge effect generated in the leading area and the trailing area is numerically different by one order. Even though the same polishing condition is applied to the entire surface of the workpiece, the distortion degree of the TIF in the leading

area and the trailing area is different because of the asymmetrical characteristic of the TIF. Different distortions of the TIF in the leading and trailing areas cause edge effects of different shapes and sizes. The edge effect in the trailing area was also simulated using the proposed model and is represented by the dotted lines in Fig. 11. The predicted edge effect using the given conditions fitted well with the rolling down characteristics shown by each polishing result. To quantitatively evaluate the proposed edge effect prediction model, the relative error, Δ, can be expressed by Eq. (7).

$$\Delta = \frac{RMS \; of \; \left| E_m - E_p \right|}{RMS \; of \; E_m} \times 100\% \qquad (7)$$

where E_m denotes the edge effect measured through experiments, and E_p signifies the edge effect predicted using the proposed model. Since the edge effects generated from the leading edge and the trailing edge are created under one polishing condition, the relative error is not calculated by dividing the leading/trailing region. Table 2 shows the geometric comparison between the edge effects generated through the MRF process and predicted through the proposed model. The maximum height shown in Table 2 indicates the deepest depth of the edge effects, and the negative sign signifies the rolled-down shape. As the proposed prediction model is the empirical function composed of the volume of edge TIFs obtained from the experiment, we reckon that the difference in height and relative error are caused by the environmental change that occurred during the experiment for edge TIFs.

In the leading area, the maximum height of the edge effect increases as the step height decreases, and the difference in

Table 2 Maximum height and relative error of edge effects

Step height, D_s (mm)	Leading area		Trailing area		Full range
	Measured max height (nm)	Estimated max height (nm)	Measured max height (nm)	Estimated max height (nm)	Relative error, Δ (%)
0.160	−0.099	−0.101	−0.013	−0.012	6.80
0.080	−0.192	−0.202	−0.025	−0.024	4.23
0.053	−0.303	−0.303	−0.034	−0.037	3.99
0.040	−0.408	−0.404	−0.050	−0.049	4.01

height between the measured maximum height and the estimated maximum height under the given conditions was calculated as 10 nm or less. In the trailing area, the step height and the maximum height were similarly observed to be inversely proportional, and the difference in height was calculated as 5 nm or less. When the experimental conditions, D_s, were 0.160 mm, 0.080 mm, 0.053 mm, and 0.040 mm, the relative errors were calculated as 6.80%, 4.23%, 3.99%, and 4.01%, respectively. The relative error tends to increase as the step height, D_s, increases. This tendency can be interpreted as when the step height is large, the amount of the measured edge effect becomes small, and the relative error increases accordingly. Considering that the distributions of the difference height are constant under the given conditions for each area and the relative errors converge to approximately 4%, the stable prediction tendency of the proposed model was confirmed.

4 Conclusions

The edge effect generated during optical component manufacturing occurs when the TIF has an overhang distance from the edge of the workpiece. In several previous studies, the edge effect was indirectly estimated by predicting the edge TIF, which is nonlinearly distorted according to the change in the overhang ratio, rather than directly predicting the edge effect. The method of predicting edge TIFs is difficult to directly simulate the edge effect that occurs after the actual polishing process because the surface after polishing depends on the process parameters, such as tool moving speed and tool rotation speed. In this study, we presented a model that could directly predict the nonlinear edge effect occurring in MRF. The edge TIFs with various overhang distances were empirically obtained and segmented at specific intervals, and the material removal volume of each segment was calculated. Each segment was used to estimate the MRA for each lateral position of the workpiece edge. Combined with the polishing parameters, the model predicted the edge effect to occur after polishing. Because this model is based on the TIF volume, it could be equally applied to the edge, where TIF is distorted, or the inside, where TIF is not distorted. MRA could be calculated based on normal TIF in the inner region, where TIF distortion does not occur, and on edge TIFs in the edge region, where TIF distortion occurs. The calculated MRA could be combined with the polishing conditions to directly predict the entire surface map, including edge effects occurring after polishing.

The experimental validation of this model was successfully performed. A uniform removal process along the raster scan path was carried out to polish the entire surface of the metallic material—electroless nickel. The relative error, Δ, for quantitatively comparing the experimental data and the predicted data was within the range of less than 10% under the given experimental conditions, indicating that about 90% of the surface error could be corrected. The prediction model had high predictive accuracy for the surface figure to be created because this method could directly predict the edge effect by combining the empirically obtained TIF and the machining parameters used for polishing. Through this study, we contributed to the experimental verification of the effect of shear force on the edge of the workpiece during the MRF process. The correlation between edge TIF and edge effect was also explained by presenting a prediction model based on the MRR change of TIF. This prediction model could be applied to various targets as it does not depend on the type and size of the material. In addition, the high predictive convergence rate for residual error after processing could contribute to the reduction of manufacturing costs and process time for large optical components in MRF. The edge effect is one of the unavoidable errors in the MRF. This study does not include an experiment to compensate for the edge effect that occurs in the MRF. If MRF technology that corrects the edge effect is developed in the future and combined with a prediction model for edge effect, significant advances in process efficiency will be achieved.

Author contributions All authors read and approved the final manuscript.

Declarations

Competing interests The authors declare that they have no competing interests.

References

1. Schneider, F., Das, J., Kirsch, B., Linke, B., & Aurich, J. C. (2019). Sustainability in ultra precision and micro machining: A review. *International Journal of Precision Engineering and Manufacturing-Green Technology, 6*(3), 601–610. https://doi.org/10.1007/s40684-019-00035-2
2. Cook, L. M. (1990). Chemical processes in glass polishing. *Journal of Non-Crystalline Solids, 120*(1–3), 152–171. https://doi.org/10.1016/0022-3093(90)90200-6
3. Brinksmeier, E., Mutlugünes, Y., Klocke, F., Aurich, J. C., Shore, P., & Ohmori, H. (2010). Ultra-precision grinding. *CIRP Annals, 59*(2), 652–671. https://doi.org/10.1016/j.cirp.2010.05.001
4. Jourani, A., Dursapt, M., Hamdi, H., Rech, J., & Zahouani, H. (2005). Effect of the belt grinding on the surface texture: Modeling of the contact and abrasive wear. *Wear, 259*(7–12), 1137–1143. https://doi.org/10.1016/j.wear.2005.02.113
5. Schinhaerl, M., Smith, G., Stamp, R., Rascher, R., Smith, L., Pitschke, E., Sperber, P., & Geiss, A. (2008). Mathematical modelling of influence functions in computer-controlled polishing: Part I. *Applied Mathematical Modelling, 32*(12), 2888–2906. https://doi.org/10.1016/j.apm.2007.10.013
6. Kordonski, W., & Jacobs, S. (1996). MAGNETORHEOLOGICAL FINISHING. *International Journal of Modern Physics B, 10*, 2837–2848. https://doi.org/10.1142/S0217979296001288
7. Kordonski, W., & Gorodkin, S. (2011). Material removal in magnetorheological finishing of optics. *Applied Optics, 50*(14), 1984. https://doi.org/10.1364/AO.50.001984
8. Jones, R. A. (1986). Computer-controlled optical surfacing with orbital tool motion. *Optical Engineering, 25*(6), 256785. https://doi.org/10.1117/12.7973906
9. Preston, F. W. (1927). The theory and design of plate glass polishing machines. *Journal of the Society of Glass Technology, 11*, 214–256.
10. Wagner, R. E., & Shannon, R. R. (1974). Fabrication of Aspherics using a mathematical model for material removal. *Applied Optics, 13*(7), 1683. https://doi.org/10.1364/AO.13.001683
11. Luna-Aguilar, E., Cordero-Davila, A., Gonzalez, J., Nunez-Alfonso, M., Cabrera, V., Robledo-Sanchez, C. I., Cuautle-Cortez, J., & Pedrayes, M. H. (2003). Edge effects with Preston equation. *Future Giant Telescopes Proceeding of SPIE*. https://doi.org/10.1117/12.459869
12. Cordero-Dávila, A., González-García, J., Pedrayes-López, M., Aguilar-Chiu, L. A., Cuautle-Cortés, J., & Robledo-Sánchez, C. (2004). Edge effects with the Preston equation for a circular tool and workpiece. *Applied Optics, 43*(6), 1250. https://doi.org/10.1364/AO.43.001250
13. Kim, D. W., Park, W. H., Kim, S.-W., & Burge, J. H. (2009). Parametric modeling of edge effects for polishing tool influence functions. *Optics Express, 17*(7), 5656. https://doi.org/10.1364/OE.17.005656
14. Liu, H., Wu, F., Zeng, Z., Fan, B., & Wan, Y. (2014). Edge effect modeling and experiments on active lap processing. *Optics Express, 22*(9), 10761. https://doi.org/10.1364/OE.22.010761
15. Shorey, A. B. (2000). *Mechanisms of Material removal in magnetorheological finishing (MRF) of glass*. University of Rochester.
16. DeGroote, J. E., Marino, A. E., Wilson, J. P., Bishop, A. L., Lambropoulos, J. C., & Jacobs, S. D. (2007). Removal rate model for magnetorheological finishing of glass. *Applied Optics, 46*(32), 7927. https://doi.org/10.1364/AO.46.007927
17. Miao, C., Shafrir, S. N., Lambropoulos, J. C., Mici, J., & Jacobs, S. D. (2009). Shear stress in magnetorheological finishing for glasses. *Applied Optics, 48*(13), 2585. https://doi.org/10.1364/ao.48.002585
18. Kum, C. W., Sato, T., & Wan, S. (2013). Surface roughness and material removal models for magnetorheological finishing. *International Journal of Abrasive Technology, 6*(1), 70. https://doi.org/10.1504/IJAT.2013.053170
19. Hu, H., Dai, Y., Peng, X., & Wang, J. (2011). Research on reducing the edge effect in magnetorheological finishing. *Applied Optics, 50*(9), 1220. https://doi.org/10.1364/AO.50.001220
20. Zhong, X., Fan, B., & Wu, F. (2020). Reducing edge error based on further analyzing the stability of edge TIF and correcting the post-edge algorithm in MRF process. *Optical Review, 27*(1), 14–22. https://doi.org/10.1007/s10043-019-00555-x
21. Pollicove, H., & Golini, D. (2003). Deterministic manufacturing processes for precision optical surfaces. *Key Engineering Materials, 238–239*, 53–58. https://doi.org/10.4028/www.scientific.net/KEM.238-239.53
22. Bingham, R. G., Walker, D. D., Kim, D.-H., Brooks, D., Freeman, R., & Riley, D. (2000). A novel automated process for aspheric surfaces. *Current Developments in Lens Design and Optical Systems Engineering Proceeding of SPIE, 4093*, 6. https://doi.org/10.1117/12.405237
23. Kim, D. W., & Kim, S.-W. (2005). Static tool influence function for fabrication simulation of hexagonal mirror segments for extremely large telescopes. *Optics Express, 13*(3), 910. https://doi.org/10.1364/OPEX.13.000910
24. Kordonski, W., & Golini, D. (2002). Multiple application of magnetorheological effect in high precision finishing. *Journal of Intelligent Material Systems and Structures, 13*(7–8), 401–404. https://doi.org/10.1106/104538902026104
25. Shorey, A. B., Jacobs, S. D., Kordonski, W. I., & Gans, R. F. (2001). Experiments and observations regarding the mechanisms of glass removal in magnetorheological finishing. *Applied Optics, 40*(1), 20. https://doi.org/10.1364/AO.40.000020
26. Ghosh, G., Dalabehera, R. K., & Sidpara, A. (2019). Parametric study on influence function in magnetorheological finishing of single crystal silicon. *International Journal of Advanced Manufacturing Technology, 100*(5–8), 1043–1054. https://doi.org/10.1007/s00170-018-2330-1

Minwoo Jeon received the Master of Applied Science from Chungnam National University at 2016. He joined Optical Instrumentation Research Center, Korea Basic Science Institute (KBSI) in 2017 as a Research Engineer. His current research interests include the ultra-precision manufacturing technology and the material removal mechanism.

Seok-Kyeong Jeong received the Master of Naval Architecture from Kunsan National University at 2016. He joined Optical Instrumentation Research Center, Korea Basic Science Institute (KBSI) in 2018 as a Research Student. His current research interests include the design and ultra-precision manufacturing technology of special surface.

Young-Jae Kim is MS candidate in the Department of Analytical Science and Technology, Chungnam National University. His research interest is ultra-precision freeform surface machining and large area optical components machining.

Jong-Gyun Kang is in the Ph.D. course of Mechanical Engineering at Chungnam National University since 2019. His current research interests include the ultra-precision manufacturing technology and spectroscopy system.

Hwan-Jin Choi is a researcher in the Center for Research Equipment, Korea Basic Science Institute. His research interests include ultra-precision freeform surface machining and large area optical components machining.

Woo-Jong Yeo received the M.E. in mechanical engineering from Chungnam National University at 2020. He is currently a Researcher with the Center for Scientific Instrumentation, Korea Basic Science Institute, Daejeon, South Korea. His current research interests include ultra-precision freeform surface machining and optical components machining.

Wonkyun Lee received his B.S. and Ph.D. degrees in Mechanical Engineering in 2008 and 2015, respectively, from Yonsei University, Seoul, South Korea. He is currently an Associate Professor at the School of Mechanical Engineering, Chungnam National University, since 2016. His research interests include precision machining, robotic machining systems, and machine tool optimization based on cyber-physical systems.